Trends in Physical Chemistry
Vol. 16, 2016

Original Communication

Thermoelectric properties of silver antimonate prepared by spark plasma sintering

Kensuke Ozawa[a], Hirofumi Kakemoto[b] and Hiroshi Irie[a,b,*]

[a]Interdisciplinary Graduate School of Medicine and Engineering; [b]Clean Energy Research Center, University of Yamanashi, 4-3-11 Takeda, Kofu, Yamanashi 400-8511, Japan.

ABSTRACT

Silver antimonate ($AgSbO_3$) and silver (Ag) composites ($Ag/AgSbO_3$) were synthesized by spark plasma (SP) sintering with the aim of realizing a thermoelectric material. The SP-sintered sample had higher relative density than normal-sintered (NS) one prepared by a conventional solid-state reaction method, reflecting its increased electrical conductivity (σ), decreased Seebeck coefficient (S), and increased thermal conductivity (κ). The increased σ contributed to an increased dimensionless figure of merit (ZT), and ZT of the SP sample was higher than that of the NP. In addition, it was proved that the formation of Sb^{3+} in $AgSbO_3$ and that of Ag and $AgSbO_3$ composite ($Ag/AgSbO_3$) played an important role in enhancing the ZT value when compared with the ZT of defective $AgSbO_3$, which included more amount of Sb^{5+} but not Ag.

KEYWORDS: electroceramics, energy conversion, thermoelectric material, silver antimonate, spark plasma sintering

ABBREVIATIONS

S	:	Seebeck coefficient
σ	:	electrical conductivity
κ	:	thermal conductivity
T	:	absolute temperature
ZT	:	dimensionless figure of merit
PF	:	power factor
TE	:	thermoelectric
SP	:	spark plasma
SSR	:	solid state reaction
NS	:	normal sintering
SPS	:	spark plasma sintering
NAT	:	nitric acid treatment

*Corresponding author: hirie@yamanashi.ac.jp

1. INTRODUCTION

Thermoelectric (TE) materials have the potential to recycle exhausted heat energy and are expected to be used to generate clean energy without polluting the environment. Recently, several oxides have been recognized as potential thermoelectric materials [1-4]. The TE conversion efficiency is represented by a dimensionless figure of merit, $ZT = S^2\sigma T/\kappa$, where S, σ, κ, and T are the Seebeck coefficient, electrical conductivity, thermal conductivity, and absolute temperature, respectively. From these equations, high S and σ values and a low κ are required for high TE performance.

Silver antimonite ($AgSbO_3$) has a defect pyrochlore structure composed of linear chains of AgO_6 and SbO_6, and possesses rather high mobility (μ) originating from its highly-dispersed conduction band composed of Ag 5s and Sb 5s orbitals [5, 6]. In addition, $AgSbO_3$ has low stacking density and thus its κ_{ph} (thermal conductivity mediated by phonons) is significantly lower than those of other oxides [7, 8]. These features are opposite to those of typical oxides with low μ and high κ_{ph}, originating from their ionic bonding between light atoms and high electronegativity of oxygen. Thus, $AgSbO_3$ has been investigated as a candidate n-type TE material; however, σ of $AgSbO_3$ is low due to the

absence of free electrons because Ag^{+} and Sb^{5+} have closed electronic configuration ($4d^{10}$). Also, the low density of $AgSbO_3$, prepared by a conventional solid state reaction (SSR) using Ag_2O and Sb_2O_5 (or Sb_2O_3) as reactants, greatly limits its σ [5, 7]. To overcome low σ, modification of $AgSbO_3$ by the formation of Ag islands [9] or addition of CuO has been performed [5], and a spark plasma (SP) sintering method has been applied to prepare dense $AgSbO_3$ [7]. The SP sintering method allows the production of dense samples as the whole preparation process is under high pressure as well as allows the rapid densification of materials because of its high heating and cooling rates. In addition, we have recently found that the nitric acid (HNO_3) treatment of $AgSbO_3$ causes Ag defects, forming $Ag_{1-x}SbO_{3-y}$ [10].

In this paper, we characterize $AgSbO_3$ in detail, and discuss the effects of the existence of Ag metallic phase, the valency of Sb ion, and relative density of a sintered body on TE properties of $AgSbO_3$, prepared by a combination of the HNO_3 treatment and the SP or SSR sintering method.

2. MATERIALS AND METHODS

$AgSbO_3$ was synthesized by SSR using Ag_2O (>99.0%, Kanto Kagaku) and Sb_2O_3 (>98.0%, Kanto Kagaku) as raw materials. The raw materials were weighed to the stoichiometric molar ratio, and were mixed by ball milling for 20 h, and then the mixed powder was calcined at 900 °C for 2 h. The calcined powder was treated by HNO_3 (5.0 mol/L, Kanto Kagaku) to remove metallic Ag and to generate Ag defects, and then dried at 90 °C for 20 h. The HNO_3-treated and non-treated powders were uniaxially pressed into a disc pellet with the dimensions ~15 mm diameter × 20 mm thickness, followed by calcination in a SP sintering apparatus (SPS-515, Fuji Denpa Kouki) under pressure of 40 MPa at three-step temperatures, 700, 750, and finally 800 °C. Each temperature step was maintained for 5 min. The obtained samples from HNO_3-treated and non-treated $AgSbO_3$ are denoted by NAT-SPS and SPS, respectively. Disk pellets after the SP sintering were cut into rectangular pellets with the dimensions ~ 5 mm × 12 mm × 12 mm for measurements of TE properties. For reference, the powder without HNO_3 treatment was uniaxially pressed into a rectangular pellet with the dimensions ~ 4 × 5 × 20 mm, followed by calcination in an electric furnace (HPM-1N, AS-ONE) in air at 900 °C for 2 h (denoted by NS, normal sintering).

The calcined powders and sintered bodies were ground and pulverized into fine powders, and then characterized by conventional X-ray diffraction analysis (XRD) with CuK_α radiation (PANalytical, PW-1700). Synchrotron radiation powder diffraction patterns were obtained at BL02B2 in SPring-8 only for the sintered bodies after pulverizing them into fine powders. The patterns were collected in the 2θ range of 3°–73° in a step scanning mode, with a step length of 0.01°. The Rietveld analyses using a RIETAN-FP software (a multipurpose pattern-fitting system) were performed on the synchrotron radiation diffraction patterns. For the analysis, the space groups Fd3m (cubic, No. A-227) and Fm-3m (cubic, No. A-225) were used as the starting structural model of $AgSbO_3$ (a = 10.23 nm) and Ag (a = 4.0857 nm), respectively. A scanning electron microscope (SEM; JSM-6500F, JEOL) was used to observe the morphology of sample surfaces. The valency of Ag and Sb ions was evaluated by an X-ray photoelectron spectroscope (XPS; Axis-Ultra, Shimadzu).

Either two or four Pt wires were attached by an Ag-conductive region to the prepared rectangular pellets to measure σ and S, respectively. The temperature dependence of S (Yokogawa, Model 7563) with a temperature gradient of 5-20 K and that of σ (Agilent Technologies, E5273A) were measured from 473 K to 873 K by conventional two-probe steady-state and four-probe methods, respectively. We then calculated the power factor (PF), as expressed by $S^2\sigma$, for each sample. A modified Harman method was used to measure ZT at 600 °C [11] and then we calculated κ by using the equation, $ZT = S^2\sigma T/\kappa$.

3. RESULTS AND DISCUSSION

3.1. Characterizations of the prepared samples

The conventional XRD pattern of calcined $AgSbO_3$, not shown here, indicated that it included the homogeneous defect pyrochlore structure. The observed diffraction patterns of NS, SPS, and NAT-SPS by synchrotron radiation are shown in figs. 1a, 1b, and 1c, respectively, which also include the calculated pattern involving $AgSbO_3$ and/or Ag,

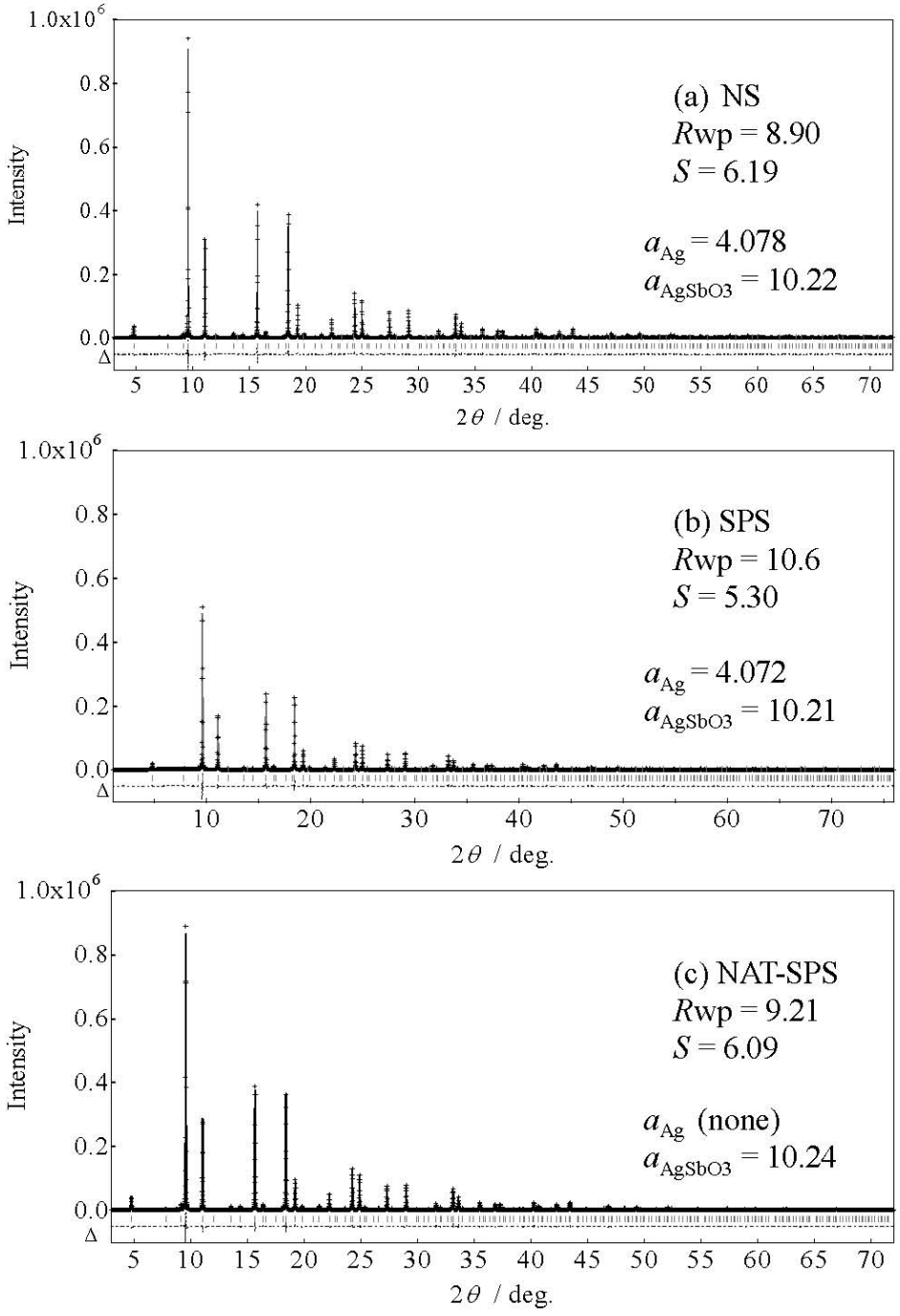

Fig. 1. Measured synchrotron radiation diffraction patterns and patterns calculated by Rietveld analysis for the prepared samples, (a) NS, (b) SPS, and (c) NAT-SPS. Crystallographic data determined by the Rietveld analysis are also included.

and Δ, representing the difference between the observed and calculated values. The molar percentages of $AgSbO_3$ and Ag in all samples, their compositions, and lattice parameters were determined by Rietveld refinement and are shown in table 1 and figs. 1a-1c. The NS and SPS samples were assigned double phases of cubic $AgSbO_3$ and Ag, whereas NAT-SPS was assigned single phase of $AgSbO_3$. The detection

of Ag was reasonably acceptable because Ag_2O is thermally decomposed to Ag at ~280 °C. In the NS and SPS samples, the Ag/Sb ratio is unity, and in good agreement with the stoichiometric ratio, although Ag exists separately in spite of the stoichiometric ratio of starting Ag_2O and Sb_2O_3. This is reasonable because Sb volatilized during sintering [5, 8]. In contrast, in NAT-SPS, the Ag/Sb ratio is less than unity, reflecting the HNO_3 treatment which extracted Ag from the $AgSbO_3$ lattice. Interestingly, the separated Ag was not detected in NAT-SPS, owing to the evaporation of Ag during SPS under the deaerated condition [11]. The relative densities of NS, SPS, and NAT-SPS pellets were 58.9, 76.7, and 74.9%, respectively (Table 1). NS had the lowest relative density, only ~60% of the theoretical one, which is considered to be attributable to the evaporation of Sb [5].

SEM images of the fracture surfaces of NS, SPS, and NAT-SPS are shown in figs. 2a, 2b, and 2c, respectively. The NS (Fig. 2a) powder, with a particle size of ~100-200 nm in diameter, appeared aggregated, indicating that it was porous. As for the SPS-treated samples, both SPS (Fig. 2b) and NAT-SPS (Fig. 2c) particles were connected with each other, i.e., "necking growth" was observed. Then, SPS and NAT-SPS became denser than NS, reflecting the increased relative density of the samples.

The binding energies corresponding to Ag $3d_{5/2}$ of Ag^0 (Ag), Ag^+ (Ag_2O), and Ag^{2+} (AgO) are 368.0–368.3, 367.6–367.8, and 367.3–367.4 eV, respectively, which are quite similar [12]. Since all the binding energies are in such a narrow range, it is hard to perform a quantitative analysis of the Ag oxidation states from a deconvolution analysis of XPS spectra with high certainty. However, qualitatively, as shown in fig. 3a, the spectrum peaks of NAT-SPS shifted to the higher energy region (inset in Fig. 3a), and also the spectrum had tailing in the lower binding energy side. These observations indicate that HNO_3-treated sample has more Ag including Ag^0 and Ag^{2+} oxidation states. The Sb $3d_{3/2}$ XPS spectra of NS, SPS, and NAT-SPS are shown in figs. 3b, 3c, and 3d, respectively. As for the oxidation states of Sb, the peaks at 540.7 and 539.7 eV are assigned to the $3d_{3/2}$ orbital of Sb^{5+} and Sb^{3+}, respectively [13]. To quantitatively evaluate the Sb^{3+}/Sb^{5+} atomic ratio, peak deconvolution was carried out using a Gaussian lineshape. The spectra

Table 1. Characterization data of NS, SPS, and NAT-SPS samples.

Sample	**NS**	**SPS**	**NAT-SPS**
Ag content / mol%	0.79	0.62	0
Composition of $AgSbO_3$ [*)]	$Ag_{1.00}Sb_{1.00}O_y$	$Ag_{1.00}Sb_{1.00}O_y$	$Ag_{0.97}Sb_{1.00}O_y$
Relative density / %	58.9	76.7	74.9
Sb^{3+}/Sb^{5+} ratio	1.5	1.7	0.53

[*)] Estimated from the occupancies of Ag and Sb in $AgSbO_3$.

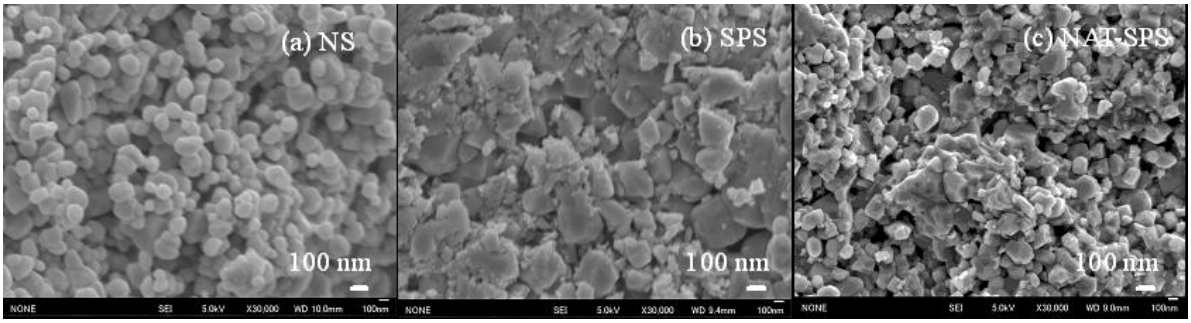

Fig. 2. SEM images of (a) NS, (b) SPS, and (c) NAT-SPS.

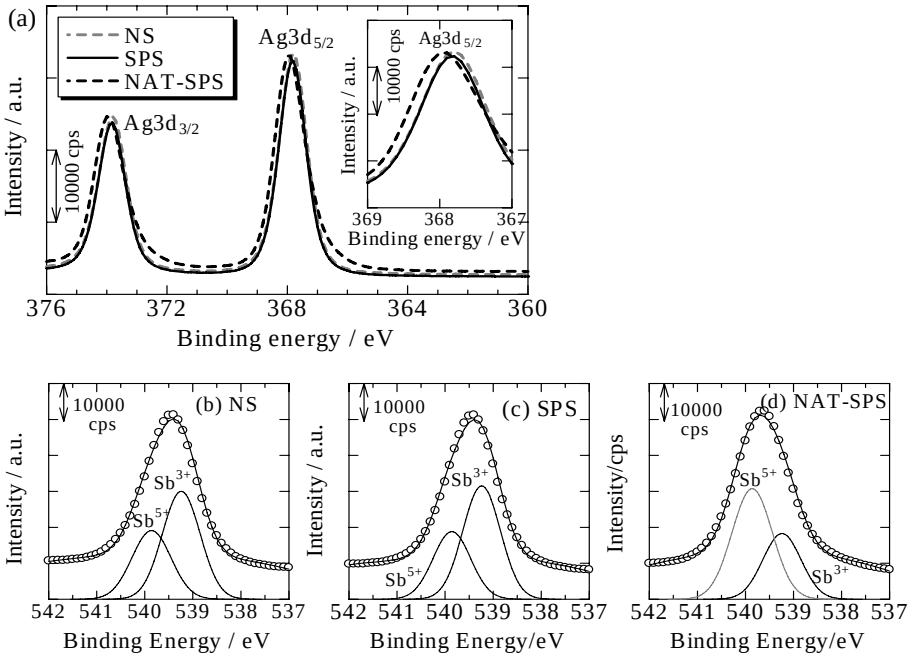

Fig. 3. XPS spectra for (a) Ag 3d (Ag $3d_{3/2}$, Ag $3d_{5/2}$), Sb $3d_{3/2}$ of (b) NS, (c) SPS, and (d) NAT-SPS. The plotted experimental data and the fitted curves closely coincided. The deconvolution curves of Sb^{3+} and Sb^{5+} are included. The Ag 3d and Sb 3d peaks were calibrated using the C 1s peak derived from the hydrocarbon surface contaminant with a binding energy of 284.6 eV.

of the component Sb^{3+} and Sb^{5+} determined by deconvolution and the fitted peaks are also shown in figs. 3b-3d. The atomic ratios of Sb^{3+}/Sb^{5+}, which were obtained by dividing the area of Sb $3d_{3/2}$ for Sb^{3+} by that for Sb^{5+}, are shown in table 1. When we compare the Sb^{3+}/Sb^{5+} ratio between SPS and NAT-SPS, more amount of Sb^{5+} was included in the HNO_3-treated sample. This is reasonable because HNO_3 acts as an oxidant. Hence, it could be considered that Ag^{2+} also increased, and then Ag^0 might increase to maintain charge neutrality.

3.2. Thermoelectric properties

Fig. 4a shows the temperature dependence of σ for NS, SPS, and NAT-SPS. All the values of σ increased with increasing temperature, which is a typical semiconductor behavior. In fig. 4a, SPS containing larger amount of Sb^{3+} and metallic Ag, and with high relative density indicated the highest σ. When we compare NS and SPS in which the amount of metallic Ag and the Sb^{3+}/Sb^{5+} ratio are quite similar, and the Ag/Sb ratios are both unity (stoichiometric ratio), $AgSbO_3$ with higher relative density showed higher σ than that with the lower density. Hence, increasing

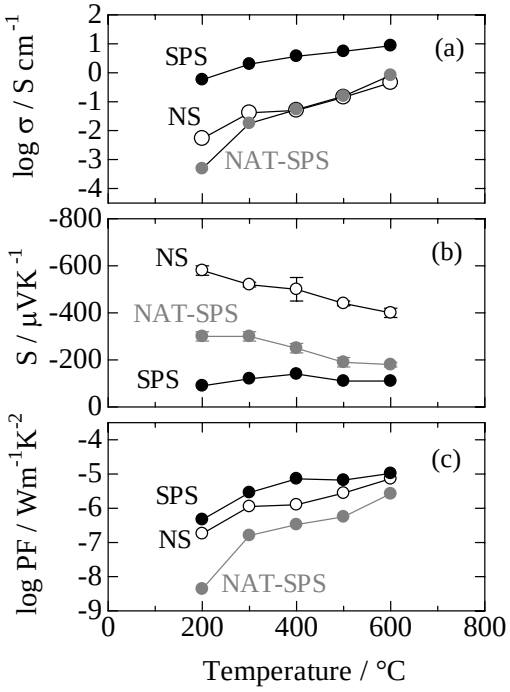

Fig. 4. Temperature dependence of (a) electrical conductivity, σ and (b) Seebeck coefficient, S, and (c) power factor, PF.

the relative density is the key to increase σ, which is understandable. When SPS and NAT-SPS having similar relative densities are compared, σ of SPS was 1~3 orders of magnitude larger than that of NAT-SPS in the measured range. In general, the metallic Ag contributes to the conduction path as bypasses for carrier transport. However, in the present study, because the SPS sample contains only 0.62 mol%, it is presumably considered that the Ag particles are not connected with each other. Thus, the metallic Ag would not be mainly responsible for the increase in σ, but for S, which will be discussed later. As mentioned above, NAT-SPS containing Ag-defect ($Ag_{0.97}Sb_{1.00}O_y$) has more amounts of Ag^0 ($4d^{10}5s^1$) and Ag^{2+} ($4d^9$) than SPS ($Ag_{1.00}Sb_{1.00}O_y$, Ag^+ ($4d^{10}$), closed electronic-shell configuration), meaning the increase in σ was due to their open electronic-shell configurations. However, the opposite experimental results were observed. Hence, producing Sb^{3+} is also the key to increase σ. This could be plausible because generating Sb^{3+} caused the generation of more oxygen vacancies in the material, and thus the corresponding donor levels are created in the bandgap. This can provide more conduction electrons than in the case of no donor levels in the gaps.

Temperature dependence of S for NS, SPS, and NAT-SPS is shown in fig. 4b. S values of all the samples were negative, indicating the occurrence of n-type conduction. The trend in the absolute values of S in SPS and NAT-SPS covered the Ioffe's theory, that is, the absolute value of S decreases when σ increases. Hence, SPS had the lower absolute value for S than NAT-SPS. However, when we compare NS and NAT-SPS, the absolute S values of NS were higher than those of NAT-SPS even though the absolute σ values of NS were higher (at 200 °C) or quite similar (at 300–600 °C), compared to those of NAT-SPS. It was considered that the increase in the amount of Sb^{3+} mainly caused the decrease in the absolute value of S because σ increases as mentioned above. Hence the existence of Ag would contribute to higher S. To enhance σ for a low-σ material, which usually has a high S value, and to realize a high TE performance, a conductive material can be dispersed at the grain boundaries of such a low-σ material, i.e., aluminum-doped zinc oxide (Al-ZnO) or Ag-doped calcium cobalt oxide (Ag-$Ca_3Co_4O_9$) [14, 15]. It is probable that a similar phenomenon occurs in the NS sample, that is, highly conductive Ag particles disperse between those of $AgSbO_3$. Another possible reason for the higher absolute S of NS than that of NAT-SPS is the lower relative density of NS than NAT-SPS. Fig. 4c shows the temperature dependence of power factor (*PF*), which was calculated from the formula $\sigma \times S^2$. The highest *PF* observed in this study (~1×10^{-5} W m^{-1} K^{-2}) was obtained for SPS at 600 °C.

Finally, we examined the *ZT* values for the NS, SPS, and NAT-SPS samples at 600 °C using the modified Harman method and then κ was calculated. The *ZT* values for NS, SPS, and NAT-SPS were 0.009, 0.011, and 0.004, respectively. The κ value for NS was calculated to be 0.42 W m^{-1} K^{-1}, which reasonably coincides with the previously reported values of 1.1 and 0.8 W m^{-1} K^{-1} at room temperature and 400 °C, respectively [8]. The κ value for SPS was 0.56 W m^{-1} K^{-1}, which is higher than that for NS, caused by the higher relative density of SPS. The κ value for NAT-SPS was 0.42 W m^{-1} K^{-1}, which is lower than that for SPS. This is attributable to the presence of Ag defects, causing the phonon scattering by the defect site, and to the absence of metallic Ag. Although these *ZT* values need to be increased by around two orders of magnitude to be preferable for practical use, this study demonstrates that the production of the dense sample, introduction of Sb^{3+} in $AgSbO_3$, and generation of metallic Ag to form Ag/$AgSbO_3$ enhance the thermoelectric properties of $AgSbO_3$.

4. CONCLUSION

We prepared three types of $AgSbO_3$-based thermoelectric materials, by combination of the NS and SP sintering methods, and HNO_3 treatment. Among them, the sample that had highest σ indicated the highest *ZT*, attributable to the generation of Sb^{3+}, the presence of conductive Ag, and high relative density, in spite of lower S and higher κ. The *ZT* value for SPS was observed to be ~0.011 at 600 °C, which is two orders of magnitude smaller than the minimum value considered to be required for practical use, which is greater than 1. To achieve a higher *ZT* value, we are now trying to dope Cu in $AgSbO_3$ using the SPS method because it is known that the optimal Cu doping allows the enhancement of TE properties.

ACKNOWLEDGEMENTS

The experiments at SPring-8 were performed with the approval of the Japan Synchrotron Radiation Research Institute (JASRI) (Proposal No. 2014A1008).

CONFLICT OF INTEREST STATEMENT

There are no conflicts of interest.

REFERENCES

1. Terasaki, I., Sasago, Y. and Uchinokura, K. 1997, Phys. Rev. B, 56, R12685.
2. Ohtaki, M., Tsubota, T., Eguchi, K. and Arai, H. 1996, J. Appl. Phys., 79, 1816.
3. Li, S., Funahashi, R., Matsubara, I., Ueno, K., Sodeoka, S. and Yamada, H. 2000, Chem. Mater., 12, 2424.
4. Ohta, H., Kim, S., Mune, Y., Mizoguchi, T., Nomura, K., Ohta, S., Nomura, T., Nakanishi, Y., Ikuhara, Y., Hirano, M., Hosono, H. and Koumoto, K. 2007, Nature, 6, 129.
5. Nishiyama, S., Ichikawa, A. and Hattori, T. 2004, J. Ceram. Soc. Jpn., 112, 298.
6. Allen, J. P., Nilsson, M. K., Scanlon, D. O. and Watson, G. W. 2011, Phys. Rev. B, 83, 035207.
7. Sang, H.-Y. and Li, J.-F. 2010, J. Alloy Comp., 493, 678.
8. Li, F. and Li, J.-F. 2011, J. Electro. Mater., 40, 1035.
9. Wiggers, H., Simon, U. and Schon, G. 1998, Solid State Ionics, 107, 111.
10. Kobayashi, R., Tanigawa, S., Takashima, T., Ohtani, B. and Irie, H. 2014, J. Phys. Chem. C, 118, 22450.
11. Kawano, T., Kakemoto, H. and Irie, H. 2015, Mater. Lett., 156, 94.
12. Melin, E. P., Diaz, O. G., Rodrigues, J. M. D., Colon, G. and Navio, G. C. 2012, Appl. Catal. B: Environ., 127, 112.
13. Zhang, H., Sun, K., Feng, Z., Ying, P. and Li, C. 2006, Appl. Catal. A: General, 305, 110.
14. Ohtaki, M., Tsubota, T., Eguchi, K. and Arai, H. 1996, J. Appl. Phys., 79, 1816.
15. Mikami, M., Ando, N. and Funahashi, R. 2005, J. Solid State Chem., 178, 2186.